SmallSat Aerocapture to Enable a New Paradigm of Planetary Missions

Alex Austin, Adam Nelessen, Bill Strauss, Joshua Ravich, Mark Jesick
Jet Propulsion Laboratory, California Institute of Technology
Pasadena, CA 91109
818-393-7521
Alexander.Austin@jpl.nasa.gov

Ethiraj Venkatapathy, Robin Beck, Paul Wercinski, Michael Aftosmis, Michael Wilder, Gary Allen
NASA Ames Research Center
Moffett Field, CA 94035
ethiraj.venkatapathy-1@nasa.gov

Robert Braun, Michael Werner, Evan Roelke
CU Boulder
Boulder, CO 80309
Bobby.Braun@Colorado.edu

Abstract— This paper presents a technology development initiative focused on delivering SmallSats to orbit a variety of bodies using aerocapture. Aerocapture uses the drag of a single pass through the atmosphere to capture into orbit instead of relying on large quantities of rocket fuel. Using drag modulation flight control, an aerocapture vehicle adjusts its drag area during atmospheric flight through a single-stage jettison of a drag skirt, allowing it to target a particular science orbit in the presence of atmospheric uncertainties. A team from JPL, NASA Ames, and CU Boulder has worked to address the key challenges and determine the feasibility of an aerocapture system for SmallSats less than 180kg. Key challenges include the ability to accurately target an orbit, stability through atmospheric flight and the jettison event, and aerothermal stresses due to high heat rates.

Aerocapture is a compelling technology for orbital missions to Venus, Mars, Earth, Titan, Uranus, and Neptune, where eliminating the propellant for an orbit insertion burn can result in significantly more delivered payload mass. For this study, Venus was selected due to recent NASA interest in Venus SmallSat science missions, as well as the prevalence of delivery options due to co-manifesting with potentially many larger missions using Venus for gravity assist flybys. In addition, performing aerocapture at Venus would demonstrate the technology's robustness to aerothermal extremes. A survey of potential deployment conditions was performed that confirmed that the aerocapture SmallSat could be hosted by either dedicated Venus-bound missions or missions performing a flyby.

There are multiple options for the drag skirt, including a rigid heat shield or a deployable system to decrease volume. For this study, a rigid system was selected to minimize complexity. A representative SmallSat was designed to allocate the mass and volume for the hardware needed for a planetary science mission. In addition, a separation system was designed to ensure a clean separation of the drag skirt from the flight system without imparting tipoff forces. The total spacecraft mass is estimated to be 68 kg, with 26 kg of useful mass delivered to orbit for instruments and supporting subsystems. This is up to 85% more useful mass when compared to a propulsive orbit insertion, depending on the orbit altitude.

Key to analyzing the feasibility of aerocapture is the analysis of the atmospheric trajectory, which was performed with 3 degree-of-freedom simulations and Monte Carlo analyses to characterize the orbit targeting accuracy. In addition, aerothermal sizing was performed to assess thermal protection

system requirements, which concluded that mature TPS materials are adequate for this mission. CFD simulations were used to assess the risk of recontact by the drag skirt during the jettison event.

This study has concluded that aerocapture for SmallSats could be a viable way to increase the delivered mass to Venus and can also be used at other destinations. With increasing interest in SmallSats and the challenges associated with performing orbit insertion burns on small platforms, this technology could enable a new paradigm of planetary science missions.

TABLE OF CONTENTS

1. INTRODUCTION

Aerocapture has long been considered a compelling technology that could significantly enhance science return or reduce costs for orbital missions to Mars, Venus, Titan, Uranus, and Neptune [1][2][3][4]. Aerocapture uses the drag from a single hyperbolic atmospheric pass to provide the

delta-V needed for orbit insertion (OI), rather than a large burn of a rocket engine. Studies suggest that, compared to propulsive OI, aerocapture using "traditional" planetary spacecraft can increase delivered payload mass by 15% at Mars, 70% at Venus, more than 200% at Titan and Uranus, and an estimated 800% or more at Neptune [2]. Aerocapture is particularly well-suited for SmallSat OI, due to the difficulty of designing and integrating a propulsion system to perform hundreds to thousands of meters per second delta-V on a small platform. Other proposed orbit insertion methods for SmallSats, such as solar electric propulsion, are potentially difficult to implement and can result in long cruise times to the destination, which can stress SmallSat hardware capabilities. Aerocapture presents a potentially fast and efficient way for small platforms to enter orbit around planetary bodies and accomplish meaningful science objectives.

In order to target a specific science orbit and account for day-of-flight uncertainties in the atmosphere, a control system is needed. Many aerocapture studies to date have focused on bank-angle lift modulation, which requires complex control algorithms and an integral propulsive reaction control system. The aerocapture technology described in this paper is drag modulation aerocapture, which shows promise of being simpler and more cost-effective than bank-angle lift methods [5]. Drag modulation aerocapture uses in-flight transformations of an entry vehicle's drag area to control the amount of deceleration produced during an atmospheric pass.

The simplest form of drag modulation aerocapture is the single-stage discrete-event architecture, which is depicted in Figure 1. One possible way to execute the single-stage discrete-event maneuver is to enter the atmosphere in a low ballistic coefficient configuration, with a large drag skirt deployed, and then to transition to high ballistic coefficient by jettisoning or folding the drag skirt. Such a single-stage discrete-event architecture was previously studied within the context of an Earth SmallSat Flight Test of Aerocapture [6]. Additional information on the fundamentals of drag modulation aerocapture can be found in Reference 5.
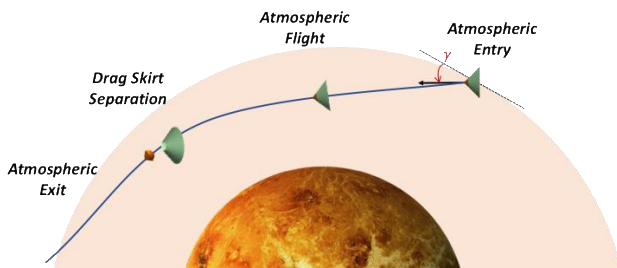

Figure 1. Single event drag modulation aerocapture is a potentially cost-effective and mass-efficient approach to achieve orbit insertion with a small satellite

The key challenges associated with drag modulation aerocapture for Small Satellites, which were the focus of this study are:

1. Vehicle stability throughout atmospheric flight, and the effects of tipoff and/or potential recontact between the two bodies after separation
2. Guidance and control architecture for targeting a precise science orbit despite navigational and atmospheric uncertainties
3. Aerothermal stresses on the vehicle due to high heat rates

In order to address these key challenges and determine the feasibility of this aerocapture system for use in SmallSat planetary missions, a multi-organizational team was formed from collaborators at the Jet Propulsion Laboratory (JPL), Ames Research Center (ARC), and the University of Colorado at Boulder (CU Boulder). Spanning various areas of expertise, this team brings a wealth of experience to address the key challenges of drag modulation aerocapture.

2. DRAG MODULATION AEROCAPTURE TRADE SPACE

The aerocapture maneuver concept of operations is made up of three main phases: exo-atmospheric coast, atmospheric deceleration, and orbit operations. There are a number of different design choices for each phase, which result in many types of mission architectures.

Exo-atmospheric Coast

Before the aerocapture maneuver begins, the spacecraft must navigate to or be brought to the vicinity of the planetary body and then target a specific entry flight path angle (EFPA) and entry velocity at the atmospheric interface. The three main delivery options identified were:

1. Direct injection of SmallSat from Earth
2. Delivery of SmallSat by host targeting the body
3. Delivery of SmallSat by host flying by the body

Option 1 provides the most flexibility for the mission, especially if the vehicle can perform the Earth escape burn from a location such as geostationary transfer orbit (GTO), as there are many launches to GTO that can carry a SmallSat as a secondary payload. The vehicle could also potentially be launched as a secondary payload with a primary mission that is going to the target body, but then released after the injection burn, similar to the MarCO spacecrafts that traveled with the InSight Mars lander. While options 2 and 3 may have more limited launch opportunities, they come with the benefit that the aerocapture vehicle does not need to be designed to perform its own interplanetary cruise, as the host could provide power and communications prior to deployment, similar to the Huygens probe that traveled with Cassini to Titan [7].

2

Atmospheric Deceleration

Once the vehicle enters the atmosphere, it begins a period of deceleration due to the drag force imparted on it. Throughout the aerocapture maneuver, the spacecraft travels hypersonically and experiences a high heating environment that requires that the exterior surface be covered in an ablative thermal protection system (TPS) material. During the maneuver, the drag skirt is jettisoned to provide control so that the vehicle can target the desired science orbit. The drag skirt is the largest component of the flight system and there are a number of potential types and configurations.

The simplest type of drag skirt is a rigid structure, similar to previously flown heatshields for missions like Pioneer Venus and the Mars Science Laboratory (MSL). A rigid drag skirt could utilize previously flown TPS materials, such as Phenolic Impregnated Carbon Ablator (PICA).

There is also the option of a deployable drag skirt, such as the Adaptable, Deployable Entry and Placement Technology (ADEPT). ADEPT employs an umbrella-like deployable structure with a "skin" that is a 3-D woven carbon fabric to serve as a TPS and as a structural surface that transfers aerodynamic deceleration forces to the underlying ribs [8][9]. The ADEPT drag skirt is made up of three primary structural elements: the carbon fabric skirt, ribs, and struts. The ADEPT structure is folded during launch and then deployed prior to atmospheric entry, which could enable the entire flight system to be packaged into a smaller volume to make it easier to launch as a secondary payload.

Orbit Operations

The final stage of the aerocapture maneuver occurs after the vehicle has exited the atmosphere. The spacecraft would now be in an elliptical orbit with the apoapsis at some altitude away from the planet and the periapsis at an altitude close to the lowest altitude seen during the atmospheric pass. For this reason, if the vehicle is left in this orbit, it will reencounter the atmosphere at the next pass through periapsis, which could result in a loss of mission. The vehicle must therefore perform a small periapsis raise maneuver (PRM) at apoapsis to bring periapsis to an altitude that is out of the atmosphere. The delta-V required for this maneuver depends on the target apoapsis altitude, but is generally ≤ 50 m/s. This maneuver can be performed with a small chemical propulsion system similar to those that have been flown or proposed for other SmallSat missions such as MarCO [10] or Lunar Flashlight [11].

3. REFERENCE MISSION CONCEPT

This study could not address all of the potential mission architectures for a SmallSat performing aerocapture, so a reference concept was identified. Venus was selected as the SmallSat destination for a number of key reasons:

- Strong potential for SmallSat scientific investigations, as seen by the compelling science missions selected in NASA's recent Planetary Science Deep Space SmallSats program [12].
- A wide variety of mission concepts frequently plan to perform gravity assists at Venus, and could deliver a small satellite to Venus' vicinity.
- Implementation at Venus would demonstrate this technology's robustness to aerothermal extremes, as Venus has a large gravity well and high heat rates. The approach and methodology developed can be later applied to other destinations such as Mars, Titan, Uranus, and Neptune.
- Transit times to Venus are comfortably within the lifetime capability of small satellite hardware

For the interplanetary cruise, the concept would seek a host spacecraft, such as a New Frontiers mission, to bring the aerocapture vehicle to the vicinity of Venus before the vehicle is jettisoned to enter the atmosphere. This method of delivery was selected to keep complexity at a minimum during initial technology development efforts, but an investigation into how the spacecraft could navigate itself to Venus is a topic of ongoing study.

The flight system would be made up of two main components: the spacecraft and the drag skirt, which can be seen in Figure 2. The spacecraft is the part of the system that remains in orbit after the aerocapture maneuver to perform the science mission. It contains all of the avionics, instruments, and other spacecraft components. For the drag skirt, a rigid design was assumed as reference, in an effort to minimize complexity, but a topic of ongoing study is to consider how an ADEPT deployable system could be used to decrease the stowed volume of the flight system and facilitate a greater number of secondary launch opportunities. A 45-degree sphere-cone geometry was selected based on heritage from Pioneer Venus (P-V) and a readily available aerodynamic database that can be used in 3-DOF simulations.
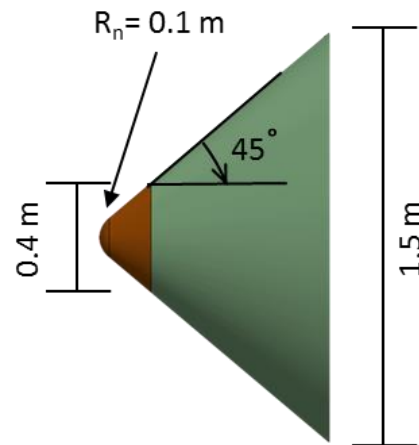

Figure 2. Aerocapture flight system with the spacecraft (orange) and the drag skirt (green)

Together, the spacecraft and drag skirt make up the "pre-jettison" configuration, which is what enters the atmosphere and has a low ballistic coefficient to decrease velocity in order to allow the spacecraft to enter into orbit around Venus. During the aerocapture maneuver, the timing of drag skirt jettison is modulated based on sensed decelerations in order to target the desired orbit. The high ballistic coefficient spacecraft becomes the "post jettison" configuration. The ratio of the ballistic coefficients between these two configurations determines how flexible the timing of the jettison event can be, with a higher value corresponding to more control authority. For the reference vehicle studied here, this ratio is approximately 7.5. The associated mass and ballistic coefficient values are summarized in Table 1.

Table 1. Summary of vehicle parameters

	Pre-Jettison	Post-Jettison
Base Diameter (m)	1.5	0.4
Mass (kg)	68.2	36.8
Drag Coefficient	1.01	1.02
Ballistic Coefficient (kg/m²)	38.1	284.9

For this aerocapture technology development effort, the mission concept remains agnostic to a specific science mission, but instead allocates the resources and adheres to requirements to accommodate an expected CubeSat/SmallSat scale instrument, which will be defined in more detail in future studies.

4. EXO-ATMOSPHERIC TRAJECTORIES AND TARGETING

Deployment Conditions Analysis

It is assumed that the spacecraft carrying the aerocapture vehicle to Venus travels on a hyperbolic trajectory relative to the planet. It is important that the aerocapture vehicle enter the atmosphere within a specific EFPA corridor, which is defined as the range of EFPA values that lead to aerocapture within acceptable orbit targeting accuracy limits.

There are two potential methods for the aerocapture vehicle to detach from the host and successfully target the atmosphere. The first assumes that the host spacecraft does not deviate from its intended trajectory and instead the aerocapture vehicle is detached using a Huygens-like spin-eject separation mechanism at some velocity and angle relative to the host spacecraft. This velocity change would cause the aerocapture vehicle to move to a different hyperbolic trajectory that intersects the atmosphere at the desired entry velocity and flight path angle. The second detachment method assumes that the host spacecraft performs a maneuver to place itself and the aerocapture vehicle on the aerocapture entry trajectory before releasing the aerocapture vehicle with a minimal delta-v. The host then

would perform a small maneuver to return to its desired trajectory. The advantage of this type of detachment architecture versus the first is that the deployment mechanism can be designed to impart a much smaller velocity and the aerocapture vehicle can be targeted more accurately at the desired EFPA, leading to greater accuracy in targeting the desired orbit. The disadvantage to this is that it puts stricter requirements on the host, which may not be willing to perform the targeting maneuvers. Both deployment methods were considered as part of this study.

In order to assess the required deployment velocity and associated coast times for the first deployment case, a parametric exploration of deployment conditions (velocity and deployment direction) was performed. This analysis used a representative host trajectory for both a Venus orbiter mission ($v_\infty = 2.9$ km/s) and a mission to the outer planets performing a gravity assist flyby ($v_\infty = 7.8$ km/s). For each of these incoming trajectories at Venus, three parameters were varied to determine what combination of deployment conditions resulted in the aerocapture vehicle entering the atmosphere at the required entry velocity and EFPA, assuming a 150 km entry altitude. These parameters were the location along the incoming trajectory where the vehicle was deployed (corresponding to the coast time to entry), the angle relative to the host spacecraft that the vehicle was deployed at, and the required delta-v that the deployment mechanism must impart on the spacecraft.

Figure 3 shows the candidate deployment conditions overlaid on curves that define the aerocapture corridor as a function of EFPA and entry velocity for a number of ballistic coefficients. The spacecraft ballistic coefficients listed in Table 1 correspond approximately to the red curves on the plot, which give an EFPA corridor width of approximately 0.4 deg, or +/- 0.2 deg. It can be seen that the candidate conditions for each type of host (orbiter versus flyby) fall into specific bins based on entry velocity, but span the range of EFPAs. The points are colored by deployment velocity from the host, which ranges from approximately 1.0 to 6 m/s.
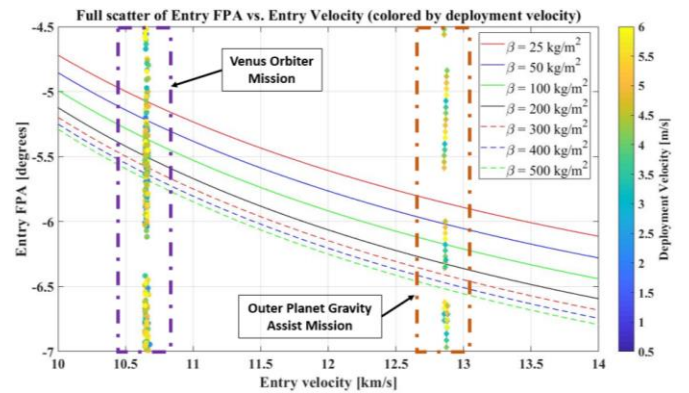

Figure 3. Potential deployment conditions overlaid on the aerocapture corridor, with points colored by deployment velocity from the host spacecraft

Figure 4 shows a similar plot, but with the points now colored by coast time of the aerocapture vehicle. This is given in hours from when the vehicle is jettisoned from the host to when it enters the atmosphere of Venus. Coast times vary between approximately 20 and 110 hours.
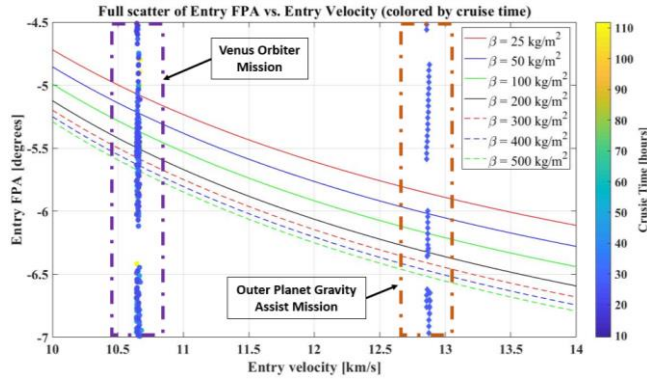

Figure 4. Potential deployment conditions overlaid on the aerocapture corridor, with points colored by coast time for the aerocapture vehicle

It is ideal for both the deployment velocity and the coast time to be small, as a small deployment will introduce less errors in the mechanical separation mechanism and a short coast time will minimize how long the aerocapture vehicle must survive on battery power, as it is assumed that solar arrays will not be exposed until after the vehicle has entered orbit. It is also important that the chosen deployment conditions lie close to the center of the required EFPA corridor to complete aerocapture successfully, as that will give the most resiliency to EFPA targeting errors. Figure 5 shows the chosen deployment conditions for both the Venus orbiter host and the gravity assist flyby host. These conditions had a deployment velocity of 3.5 m/s and 3.0 m/s with a coast time of 24.2 hours and 20.6 hours, respectively.
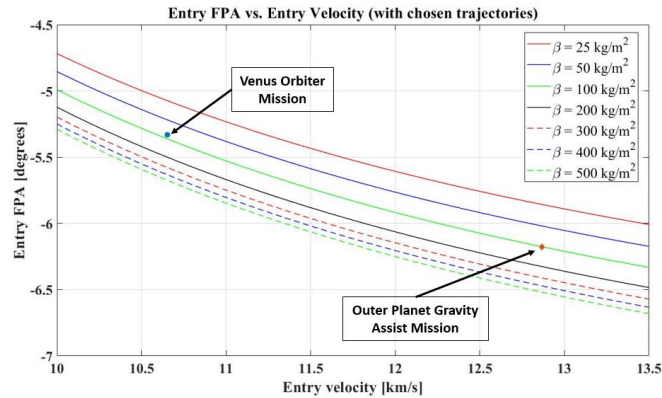

Figure 5. The deployment conditions were chosen to be centered in the EFPA requirements and have a small deployment velocity and coast time

Targeting Accuracy Analysis

With deployment conditions selected, the next thing to assess is the expected uncertainty in EFPA at the atmospheric interface. As the vehicle will be released approximately 24 hours before entry, any errors in the deployment will propagate over time and could cause the EFPA to move out of the bounds required for the aerocapture maneuver to be successful. Figure 6 shows the expected EFPA uncertainty with the assumption that the deployment mechanism imparts a 10 cm/s spherical deployment error on the spacecraft. The EFPA uncertainty also assumes Keplerian dynamics and that dispersions in the B-plane grow linearly with elapsed time from the deployment.
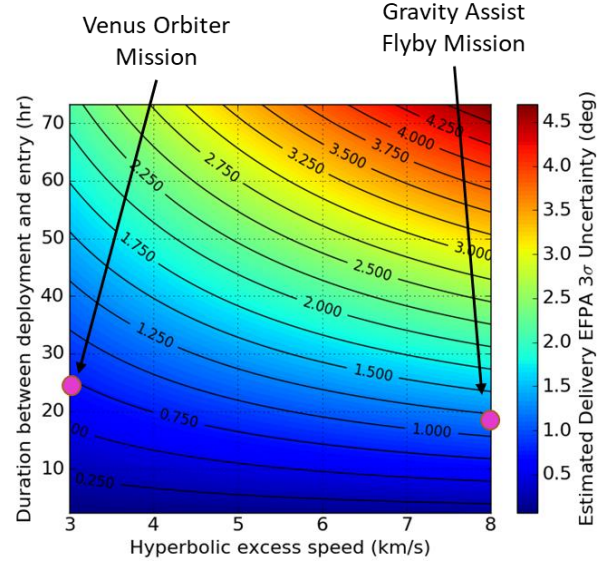

Figure 6. Expected EFPA uncertainty for the two candidate missions is shown with a 10 cm/s spherical deployment error

The results are a function of the hyperbolic excess velocity and the coast time, with the two candidate deployment conditions called out. It can be seen that the EFPA uncertainty for the Venus orbiter host spacecraft is +/- 0.75 deg and the EFPA uncertainty for the gravity assist flyby mission is +/- 1.25 deg. These are not within the bounds of approximately +/- 0.2 deg that is required for aerocapture, so the error in the deployment mechanism would need to be made less. In this case, the EFPA uncertainty scales linearly with deployment error, so we can conclude that the maximum deployment error that could be tolerated would be about 2.5 cm/s. In principle, designing a mechanical separation mechanism to impart 3 – 3.5 m/s with such a small error is difficult and not a focus of this study. Therefore, we conclude from these results that the first option of deploying from a host that does not target the aerocapture vehicle may not be the best method and instead focused on the second option where the host spacecraft targets the vehicle and releases it. A topic of ongoing study is focused on assessing how the vehicle could be designed to complete its own interplanetary cruise, which would eliminate the need for a host spacecraft and increase the number of launch opportunities.

Figure 7 shows the EFPA uncertainty for a representative Venus probe mission, assuming that the host spacecraft targets the aerocapture vehicle on the correct trajectory, releases it with a small delta-v (with a 2 cm/s spherical deployment error), and then performs a divert maneuver back

to the desired trajectory for that mission. The results are a function of how early the aerocapture vehicle is released before entry and also when the host spacecraft performs a final trajectory correction maneuver (in this example with a spherical maneuver execution error of 1 cm/s). It can be seen that for coast times as long as four days the EFPA uncertainty is within the required +/- 0.2 deg. For this study, a specific deployment time was not selected, but rather the analysis demonstrates flexibility to the host spacecraft to deploy the aerocapture vehicle when it is most convenient and least risky for them, as long as it is within four days of entry, for this example Venus flyby mission.
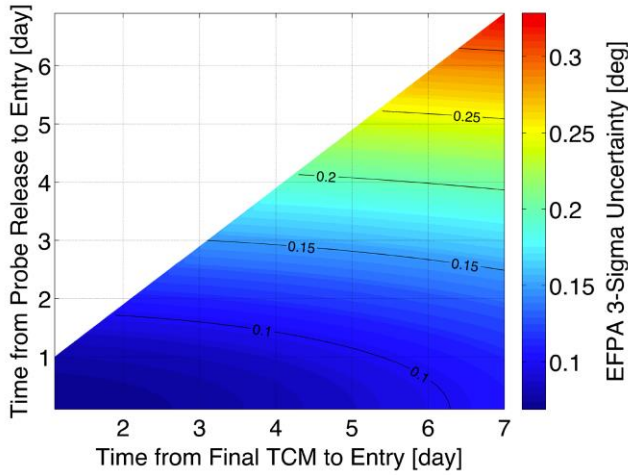

Figure 7. Expected EFPA uncertainty for the deployment case where the host spacecraft targets the aerocapture vehicle is within requirement of +/- 0.2 deg

5. ATMOSPHERIC MODELING AND MONTE CARLO SIMULATIONS

Modeling Overview

The simulation suite used for modeling atmospheric trajectories was the JPL Dynamics Simulator for Entry Descent and Surface landing (DSENDS) [13]. DSENDS has been used on previous flight missions such as MSL, Phoenix, Cassini, and on previous concept studies for aerocapture at Mars and Titan. DSENDS can be used for modeling both 3 degree-of-freedom (3-DOF) and 6-DOF dynamics, but for the results of this paper only 3-DOF dynamics were used.

The aerodynamics model used for the simulations was referenced from the Pioneer Venus aerodatabase [14]. Over the range of high Mach numbers seen in the aerocapture simulations, the Pioneer Venus axial aerodynamic coefficient was a constant value of 1.05. Although the Pioneer Venus aerodynamic model provided a set of moment coefficients allowing for the computation of 6-DOF dynamics, for simplicity it was decided that a drag only model was sufficient at this stage of the study. Because the spacecraft center of gravity is aligned with the spin-axis, the expectation is that the capsule will trim about a zero degree angle of attack during aerocapture. Therefore, the assumption was that

uncertainties in the trajectory due to oscillations in angle of attack would average out to zero over the duration of the aerocapture pass.

The atmosphere model used in the simulations was VenusGRAM [15] from Marshall Space Flight Center. The VenusGRAM model provides atmospheric density, temperature, pressure, and winds as a function of altitude, latitude, longitude, and epoch. The VenusGRAM Fortran code interfaced directly with DSENDS such that atmospheric data was queried at each time step using a current trajectory state. This allowed the DSENDS simulation to access changing atmospheric conditions during aerocapture due to variations in location over the planet, in addition to altitude variations.

The Venus gravity model included the point mass gravity term and the first two oblateness terms, J2 and J3. A third-body perturbation effect for the Sun's gravity was also included.

Numerical Predictor Corrector

The time to separate the drag skirt was computed using a guidance system employing a numerical predictor-corrector (NPC) algorithm [5]. An inertial measurement unit (IMU) model [16] provides sensed accelerations to the NPC, which are then integrated with the 3-DOF equations of motion to atmospheric exit (150 km altitude) using a 4th order Runge-Kutta integrator. A point mass gravity model was used with the integrator. The atmosphere model was a table of nominal altitude vs density created using the DSENDS nominal trajectory VenusGRAM output. At the time of drag skirt separation, the drag area, mass and drag coefficient were updated with post-jettison values. Prior to separation, the Runge-Kutta integration was performed at 10 Hz, the same rate as the DSENDS integrator, and after separation the NPC integration rate was increased to 1 Hz. Therefore, the accuracy at which the separation time could be estimated was no less than 0.1 sec.

The NPC algorithm begins its estimation of the drag skirt separation time when the sensed atmospheric acceleration is above a specified threshold value of 0.5 m/s^2. Starting with an initial guess of the separation time, the algorithm integrates the initial spacecraft state to atmospheric exit and computes the capture orbital elements using the final estimated state. If the eccentricity of the capture orbit is negative, indicating a hyperbolic trajectory, then the estimate of the separation time is increased in increments of 1.0 sec until the apoapsis altitude exceeds the target by a specified maximum tolerance. Then, the separation time is adjusted using smaller time steps of 0.1 sec. If the apoapsis altitude is above target altitude then the separation time is increased, and if the apoapsis altitude is below the target then the separation time is decreased. A solution is reached when the delta between the estimated and target altitude is within the specified minimum tolerance.

The selection of minimum apoapsis tolerance varied depending on the selection of target orbit apoapsis altitude, with the 2000 km target apoapsis tolerance set to 50 km and the 35000 km target set to 150 km. In addition, a tolerance on the rate of change of apoapsis had to be implemented in order to stop the iteration when a solution could not be reached within the specified tolerance. Lastly, a maximum separation time constraint of 200 sec had to be enforced for cases that were unable to find a solution. For the purposes of this study, an iterative approach to the solution of the target apoapsis was chosen over a faster method such as the bisection method. This option was selected due to the percentage of cases (< 5%) for which convergence on the target apoapsis was not possible. In dispersed shallow entry cases where the apoapsis altitude solution was much higher than the target, the estimated solution reached an asymptote whereby no upper bound on the solution could be determined. The bisection method requires both an upper and lower bound on the solution to converge, and therefore ~5% of the cases would not have had a solution if the bisection method was employed. The iterative method allowed for the inclusion of results for a 'best possible' capture orbit apoapsis when the target apoapsis could not be reached. A more flight-like solution solver will need to be employed in future simulations.

Atmospheric Density Estimation

In order to account for uncertainties in the atmospheric density encountered in VenusGRAM or in the actual atmosphere on the day-of-flight, a density scale factor is estimated for use in the NPC algorithm. The current density is estimated using the IMU accelerations and navigation velocity using the formulation described in Reference 5. The density scale factor is computed by dividing the estimated density by the nominal density read from the 'onboard' table. A low pass filter is used to reduce noisy atmospheric data and computes a density that is more representative of the mean value of the previous several simulation cycles.

A dispersed VenusGRAM density profile is shown in Figure 8 along with the NPC derived density scale factor. The filter provides a good balance between reducing noise and capturing short period density changes. Although the application of the density scale factor improves the estimate of current dispersed density, after the drag skirt is separated there is no longer any control available to manage the atmospheric uncertainties. Following drag skirt separation the stochastic noise or short period density changes will cause the atmospheric trajectory uncertainties to increase.

Nominal Trajectory Overview

A plot of the nominal trajectory is shown in Figures 9 and 10 for an entry velocity of 11.0 km/sec, $\beta_2/\beta_1 = 7.5$, and EFPA = -5.45 deg, targeted to an apoapsis altitude of 2000 km. The spacecraft reduced its approach velocity to below 7.7 km/sec, reaching a minimum altitude of 100 km.
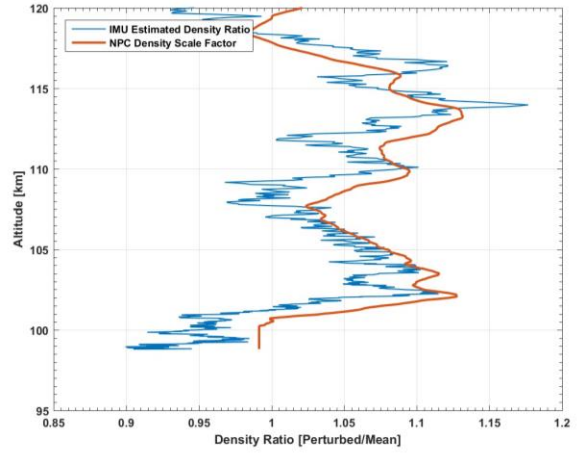

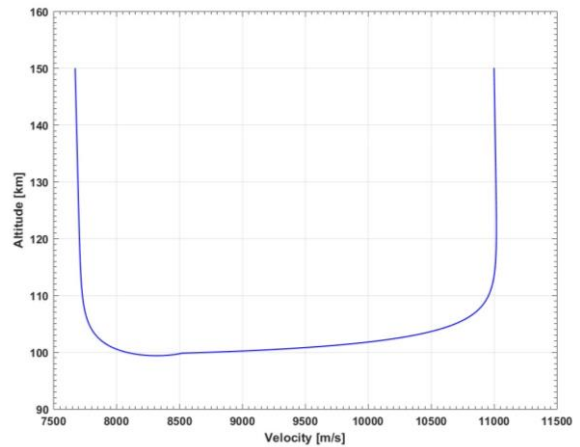**Figure 8. DSENDS VenusGRAM Perturbed Density Profile and NPC Filtered Density Scale Factor**

Figure 9. Nominal Aerocapture Trajectory Altitude vs Velocity

The maximum aerodynamic deceleration for the nominal trajectory was 8 g. The optimal time for drag skirt separation computed by the NPC algorithm was 98.7 sec, occurring approximately 5 seconds after peak deceleration.
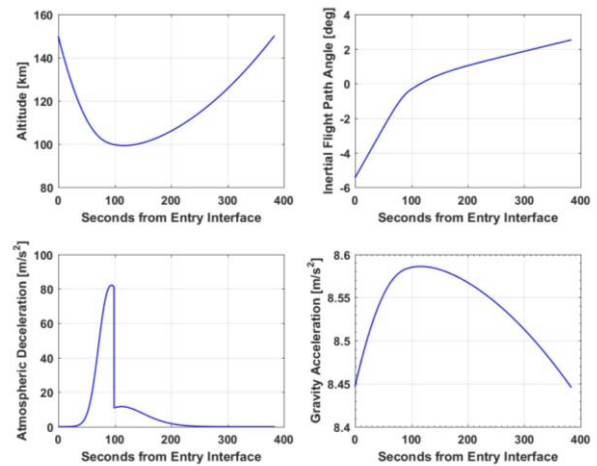

Figure 10. Nominal Aerocapture Trajectory for Target Apoapsis = 2000 km

The Monte Carlo simulations includes uncertainties due to entry state, aerodynamics, atmosphere, and sensors. A summary of the Monte Carlo simulation inputs and uncertainties is shown in Table 2. For each Monte Carlo, the ballistic coefficient β_1 prior to drag skirt separation was 38.12 kg/m^2 and the ballistic coefficient β_2 following separation was 284.9 kg/m^2 equivalent to a ratio $\beta_2/\beta_1 = 7.5$. There were 8000 dispersed cases used in each of the Monte Carlo runs described in this paper.

A +/-5% 3-σ uncertainty was applied to the drag coefficient before and after drag skirt separation. This level of uncertainty is typical of ballistic entry vehicles used on flight missions such as MER and Phoenix. The assumption is that computational fluid dynamics (CFD) analysis and ballistic range testing will have been performed in order to have confidence to +/- 5% uncertainty.

The atmospheric density and wind dispersions were generated using VenusGRAM. At each time step the VenusGRAM model generates a dispersed value of density and winds that are within the model defined 3-σ bounds [17]:

GRAM Output value = mean value + large-scale perturbations + small scale perturbations

where the large scale perturbations are variations in the profile over the entire range of altitudes for the trajectory latitude and small scale perturbations are stochastic noise applied at all altitudes along the trajectory. Although the noise perturbations are random, they are correlated across several time steps linking the variations to past dispersions. A plot of the VenusGRAM Monte Carlo density and wind perturbations is shown in Figure 11, along with the +/- 3σ boundaries provided by VenusGRAM. The density uncertainties range from +/-40% at the entry interface, 150 km altitude, to +/-25% at the drag skirt separation altitude of 100 km.

There were no dispersions on mass or center of gravity. It was assumed that, by day-of-launch, the spacecraft would have been weighed with the equivalent accuracy of previous flight missions and therefore uncertainties would have a negligible contribution to trajectory dispersions.

The estimated time needed for the drag skirt to separate from the spacecraft was uniformly dispersed from 0.05 to 0.2 seconds. This includes both the time for the mechanism to separate the drag skirt and the time for the drag skirt to physically distance itself from the capsule body. The nominal separation time and uncertainties were estimated using analytical kinematics. Future separation modeling will incorporate CFD simulations results.

Table 2. Summary of Monte Carlo Inputs

Parameters	Nominal	Dispersion
Number of Cases	8000	
Integration speed	10 Hz	
Vehicle Before Sep		
Mass, kg	68.22	Perfect
Area, m^2	1.7671	-
Cd	1.0127	5% 3-σ
β_1, kg/m^2	38.12	
Vehicle After Sep		
Mass, kg	36.82	Perfect
Area, m^2	0.1257	-
Cd	1.0284	5% 3-σ
β_2, kg/m^2	284.91	
β_2/β_1	7.47	
Nose Radius, m	0.10	
Target Conditions		
Apoapsis Altitude, km	2000.00	
Periapsis Altitude, km	200.00	
Entry State		
Entry Velocity, km/sec	11.00	0.5 m/s 3-σ
Entry FPA, deg	-5.45	+/- 0.2 3-σ
IMU		
Bias, g		0.05e^{-6} 3-σ each axis
Noise m/s		3.7e^{-3} 3-σ each axis
Scale Factor		3.0e^{-4} 3-σ each axis
Mechanical		
Mass properties		Perfect knowledge
Deploy Time, sec	0.10	-0.05 to 0.2 sec uniform
Environmental		
Density and Wind		VenusGRAM 3-σ
Venus Gravity, m^3/s^2	3.24859e^{14}	-
Sun Gravity, m^3/s^2	1.32712e^{20}	On

Uncertainties in IMU noise, bias, and scale factor were defined by the manufacturer of a potential IMU and incorporated into the simulation. The effects of IMU bias over temperature gradients were not included and will require further analysis. No uncertainties in IMU mounting location and alignment were included.
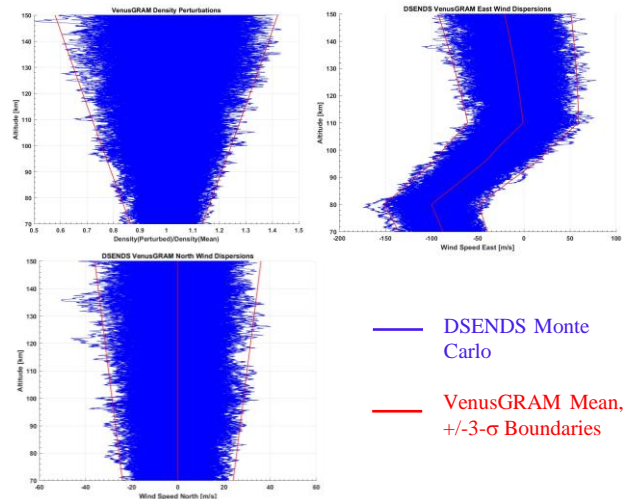

Figure 11. VenusGRAM Monte Carlo Dispersions

Navigation uncertainties included EFPA dispersions of +/- 0.2 deg 3-σ and entry velocity dispersions of 0.5 m/s. The +/- 0.2 deg flight path angle dispersions were determined to be within the capabilities of previous flight systems such as MSL. Perfect knowledge of the navigated state was used in the NPC algorithm.

Monte Carlo Results of Varying EFPA Error

Monte Carlo simulations were performed using varying levels of EFPA error in order to assess entry corridor targeting capability. A summary of the Monte Carlo results for a capture orbit apoapsis altitude of 2000 km with EFPA dispersions varying from +/- 0.1 to 0.4 deg 3-σ are shown in Table 3. The success rate of each Monte Carlo was based on the percentage of cases out of 8000 that met desired requirements. If the capture orbit altitude at periapsis was less than zero km then the spacecraft was expected to have crashed into the planet. For cases that captured into a very low periapsis altitude (< 90 km), then a maximum 0.75 kg fuel allocation to perform the periapsis raise maneuver was the limiting success criteria. Lastly, a peak heating rate requirement of 1 kW/cm^2 was imposed by the heatshield design.

Less than 1% of the cases crashed into the planet for EFPA dispersions ≤ +/- 0.3 deg 3-σ. Less than 2% of the cases failed due to peak heating rate for EFPA dispersions ≤ +/- 0.4 deg 3-σ. As the EFPA error increased, a higher percentage of the steeper dispersed entry trajectories failed either by crashing into the planet or by failure of the heatshield.

Success criteria for the cases that captured into orbit were categorized by the error in the apoapsis altitude relative to the target altitude of 2000 km. The desired requirement was that the apoapsis altitude error was less than +/- 500 km for 80% of the cases and less than +/- 1000 km for 90% of the cases. Therefore, it was determined that the maximum allowable EFPA error to satisfy all requirements was +/- 0.2 degrees 3-σ.

A plot of the NPC predicted and actual apoapsis error is shown in Figure 12 as a function of EFPA for the case with +/- 0.2 deg 3-σ uncertainty. Cases with apoapsis altitude error of approximately -2000 km have failed to reach capture orbit.

Cases where the NPC predicted apoapsis error was much larger than the target 2000 km were shallow entry cases that were unable to reach a solution within the specified tolerance but were still able to capture into a high apoapsis orbit.
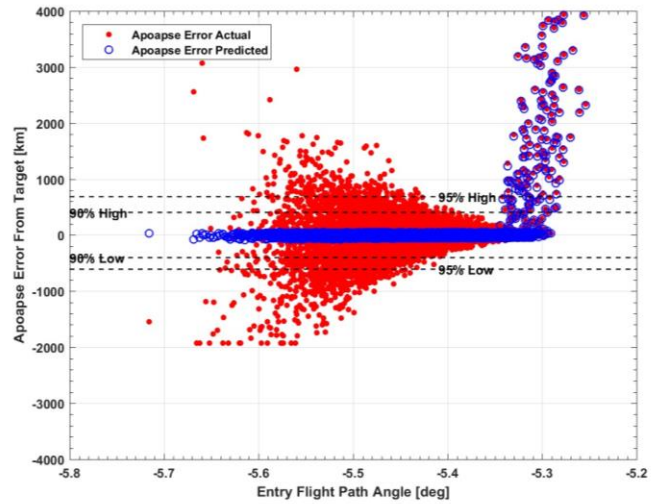

Figure 12. Apoapsis Error, NPC predicted and Actual vs. Entry Flight Path Angle

Figure 13 is a plot of the predicted and actual apoapsis error as a function of drag skirt eject time. There were a few hundred cases where the drag skirt eject time was the maximum allocated 200 sec, These cases corresponded to the shallow dispersed entry cases for which the NPC was unable to find a solution within tolerance. In general, cases with early drag skirt eject times had larger apoapsis errors due to more time being spent within the atmosphere without the benefit of the drag skirt to control atmospheric uncertainties. Shallower entry trajectories require the drag skirt to remain attached for a longer period-of-time, thus reducing apoapsis altitude errors. However, a limit is reached when there is not a sufficient amount of drag on the vehicle to accumulate the desired amount of delta-v to capture into the target orbit, as is shown for the cases where the predicted solution did not achieve the target capture orbit apoapsis.

Table 3. Monte Carlo Success Criteria (#Cases out of 8000) for Varying Entry Flight Path Angle Error

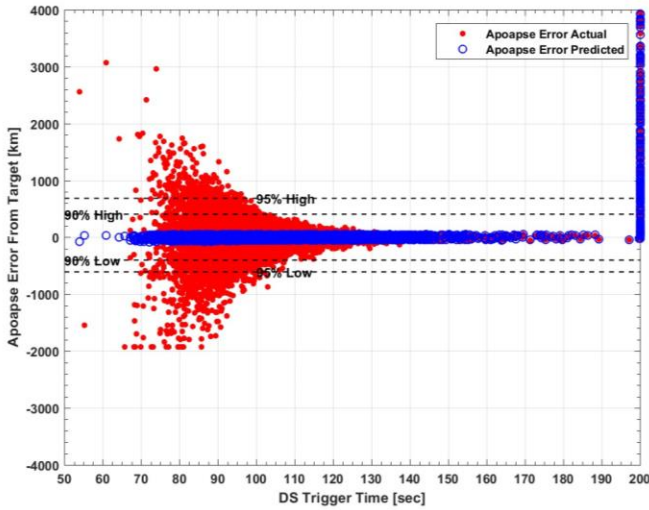| EFPA Error +/- deg 3-σ	# Cases Altitude Periapse < 0.0 km	% Cases Altitude Periapse < 0.0 km	# Cases Fuel Used > 0.75 kg	% Cases Fuel Used > 0.75 kg	Apoapsis Error 95% Low km	Apoapsis Error 90% Low km	Apoapsis Error 90% High km	Apoapsis Error 95% High km	# Cases Max Heat Rate > 1.0 kW/cm^2	% Cases Max Heat Rate > 1.0 kw/cm^2
0.10	0	0.00	0	0.00	-449.4	-329.6	308.8	445.4	0	0.00
0.15	5	0.06	7	0.09	-527.4	-361.8	332.7	492.9	0	0.00
0.20	15	0.19	28	0.35	-608.3	-401.3	405.8	685.7	1	0.01
0.25	37	0.46	51	0.64	-700.5	-445.5	588.0	1419.4	6	0.08
0.30	59	0.74	78	0.98	-836.7	-506.0	1014.0	3867.6	25	0.31
0.40	173	2.16	203	2.54	-1102.2	-652.4	4334.8	12175.1	105	1.31

Figure 13. Apoapsis Error, NPC Predicted and Actual vs. Drag Skirt Eject Time

A summary of the Monte Carlo statistics for dispersed EFPA +/- 0.2 deg 3-σ is shown in Table 4. The 99% high deceleration was 10.8 g's. The 30 m/s delta-v necessary for the periapsis raise maneuver results in a fuel allocation of 0.6 kg, within the 0.75 kg used to size the fuel tank. The 99% high stagnation point convective heating rate was 726.4 W/cm^2 and the integrated heat load was 74.1 kJ/cm^2. The orbit inclination errors were minimal at 0.04 deg.

Table 4. Summary of Monte Carlo Results

Parameter	Nominal	90%	95%	99%
Peak Deceleration, g	8.36	10.13	10.36	10.76
Max Conv. Heating Rate, W/cm^2	449.5	543.0	603.1	726.4
Integrated Heat Load, kJ/cm^2	51.47	63.48	66.82	74.13
Stagnation Pressure, kPa	7.38	11.73	13.49	17.80
Periapsis Raise Delta-V, m/sec	27.87	29.14	29.78	32.66
Periapsis Raise Fuel Used, kg	0.490	0.512	0.524	0.575
Orbit Inclin, [deg]	0.000	0.026	0.030	0.041

Monte Carlo Results of Varying Apoapsis Target Altitude

Monte Carlos were performed for capture orbit apoapsis altitudes varying from 2000 km to 35000 km to determine the impact on apoapsis targeting errors for higher capture orbits. The apoapse errors as a function of capture orbit are plotted in Figure 14. For each target apoapsis, the target EFPA was optimized in order to minimize apoapsis errors. For each case, +/- 0.2 deg 3-σ EFPA dispersions were assumed. As the target apoapsis altitude increased, it was necessary to use shallower EFPA targets in order to minimize apoapsis altitude dispersions.
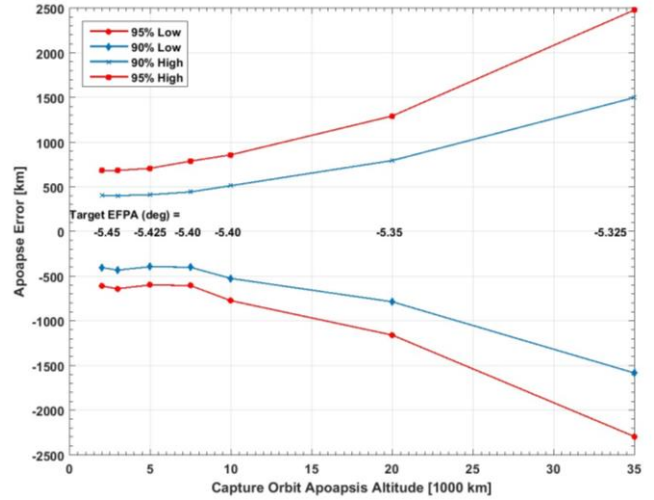

Figure 14. Apoapsis Error vs Target Apoapsis Altitude

Because higher target orbit apoapsis will naturally have larger absolute errors in kilometers of altitude, a better criterion for comparison between the target orbits are given as percent relative apoapsis errors with respect to the target, as shown in Figure 15:

Relative Apoapsis Error = (Apoapsis Altitude – Target Altitude) / Target Altitude x 100%
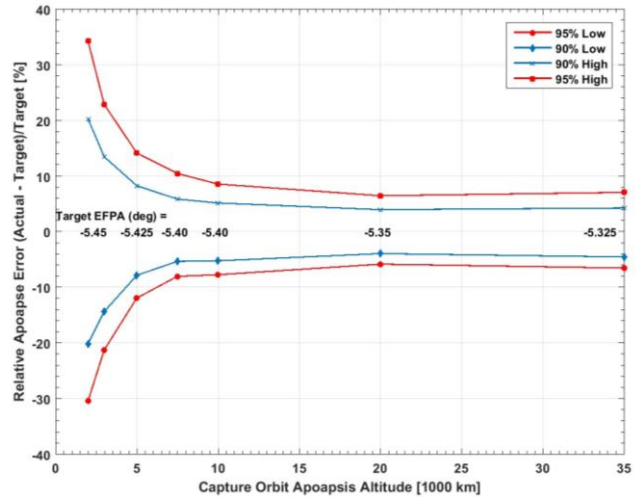

Figure 15. Relative Apoapsis Error [%] vs Target Apoapsis Altitude

As the target apoapsis altitude increases, the percent apoapsis error decreases. Plotted in Figure 16 is the delta-v and time from drag skirt eject to atmospheric exit as a function of capture orbit apoapsis. Because the amount of delta-v needed to capture decreases with increasing target apoapsis altitude, the amount of time required in the atmosphere also decreases. Therefore, the benefit of less time spent in the atmosphere following drag skirt separation results in a reduction in the effect of atmospheric dispersions.
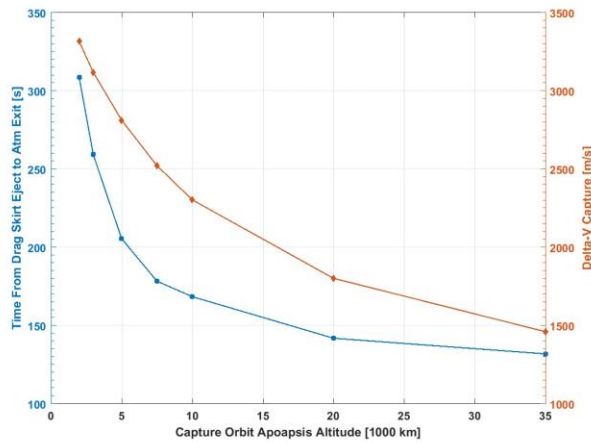
10

Figure 16. Delta-v and Time from Drag Skirt Eject to Atmospheric Exit vs Target Apoapsis Altitude

6. HEATING ENVIRONMENT AND THERMAL PROTECTION SYSTEMS

Heating Environment Overview

The heating environments were developed using the NASA Ames 3-DOF simulation code TRAJ [18]. TRAJ is a preliminary engineering software package intended as a design tool for spacecraft thermal protection systems. TRAJ combines a conventional 3-DOF trajectory simulation module, an equilibrium thermodynamics module, a stagnation point convective and radiative heating module and a one-dimensional material thermal response module into a single framework. TRAJ can be used to calculate entry trajectories, aerothermal heating, and TPS thickness and mass for both direct atmospheric entry and aerocapture simulations. Numerous generic shapes and actual planetary probes are supported, along with arbitrary geometries defined by external aerodynamic databases. The user can simulate entries at Venus, Earth, Mars, Titan, Saturn and Pluto. The software package is intended to simplify the high-fidelity process one would use to develop a detailed design of an entry vehicle, allowing the user to perform conceptual studies that provide first-order estimates of TPS requirements for proposed atmospheric entry or aerocapture missions as a function of material and trajectory design parameters. TRAJ allows for very rapid entry or aerocapture calculations in order to characterize the design space and estimate the feasibility of a mission concept.

Based on the mission concept described earlier, an entry velocity of 11 km/s and an EFPA of -5.5 deg was used in TRAJ as the entry condition at 150 km altitude. The vehicle was modeled as a 45 deg sphere cone with a 0.1 m nose radius and a 0.2 m base radius, similar nose-to-base radius ratio to the Pioneer Venus entry vehicle geometries. The drag skirt (also at 45 deg) extended the diameter of the initial entry vehicle to 1.5 m. The masses used for the TRAJ analyses were 34.7 kg for the spacecraft post-jettison configuration and 72 kg for the pre-jettison configuration. Starting with

given body geometries, TRAJ utilized entry velocity and flight path angle to determine the optimum drag skirt eject time of 92.5 sec, which occurred at 99.4 km altitude, to result in a 2000 km apoapsis orbit. These values differ slightly from those found with DSENDS and discussed in Section 5, but they are within family. Figures 17 and 18 show the TRAJ calculated acceleration on the vehicle and stagnation point heating and pressure for the trajectory.

It should be noted here that the use of heating correlations in TRAJ are valid for continuum flows. The aerocapture trajectory at high altitude and low atmospheric density, combined with the relatively small nose diameter, will result in the flow being in the transitional regime and hence the heating predictions are expected to be conservative.
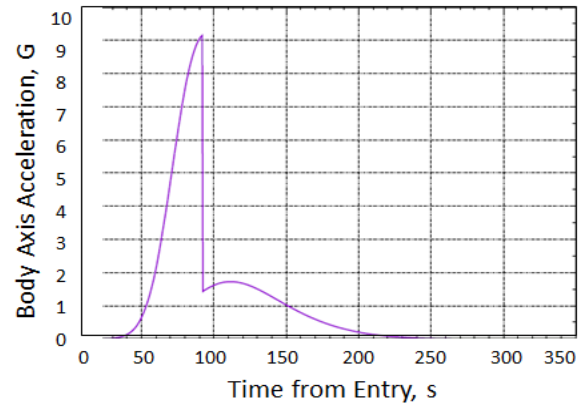

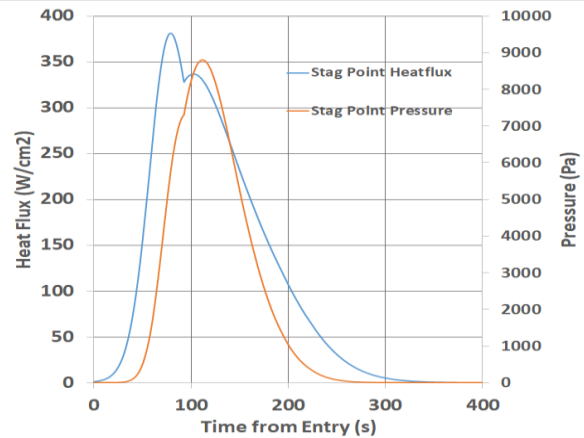**Figure 17. Acceleration vs time for the aerocapture vehicle, calculated with TRAJ**

Figure 18. Stagnation point heating and pressure vs time for the aerocapture vehicle, calculated with TRAJ

Thermal Protection System Sizing and Options

The TPS sizing module in TRAJ is FIAT [19], a one-dimensional fully implicit ablative material analysis tool. The boundary conditions, derived in the heating module were used to size TPS. Based on the fairly low (compared to Pioneer Venus) peak values of the heat flux and the pressure expected on the vehicle, low density Phenolic Impregnated Carbon Ablator (PICA), or the conformal version of PICA, C-PICA, could be used for TPS on the vehicle. Flight proven PICA is processed using a rigid, brittle reinforcement,

11

Fiberform®, while C-PICA is processed using a flexible reinforcement. The processed C-PICA is rigid, however it has a much lower thermal conductivity than PICA. It also has a much higher strain-to-failure than PICA, allowing for direct bonding onto more structural materials than PICA. C-PICA is currently a TRL 5+ technology.

For sizing, the TPS was divided into three sections: the nose, the SmallSat flank, and the drag skirt. The TRAJ stagnation point heating and pressures were used for sizing the nose. The TRAJ stagnation values were halved for the 45 deg flank and drag skirt, based on CFD analyses on 45 deg sphere-cone geometries. The TPS thicknesses for the nose and flank of the SmallSat were determined using the full heat pulse. The TPS thickness for the skirt was determined using only the heating up to jettison, because it only needs to survive until that point. The resulting environments and TPS thickness and mass on each of the TPS sections are shown in Table 5.

Table 5. Environments and TPS sizing results

	Nose	Flank (est)	Skirt (est)
Peak heat flux (W/cm²)	383.30	191.65	191.65
Peak Heat Load (J/cm²)	45179	22590	3840
Peak Pressure (Pa)	8800	4400	3650
C-PICA thickness (cm)	2.58	1.88	0.72
PICA thickness (cm)	4.125	3.51	1.11
C-PICA mass (kg)	0.13	0.80	4.56
PICA mass (kg)	0.20	1.45	6.83

The values in Table 5 were determined for un-margined laminar environments. Typically, for an actual mission, Monte Carlo analyses of the trajectory would be culled for the 3-sigma high heat flux trajectory (to determine which TPS materials to consider) and the 3-sigma high heat load trajectory to use for TPS sizing. The 3-sigma high heat load trajectory would then be evaluated with a CFD code to determine the unmargined boundary conditions used in sizing. Margining would be added to those conditions to account for uncertainties and unknowns. For this analysis, the nominal, undispersed trajectory and resulting heating was used for TPS sizing, leading to total unmargined masses of PICA and C-PICA of 8.48 kg and 5.49 kg. For mass and design considerations, the masses and thicknesses were later doubled to account for margins and uncertainties.

7. NOTIONAL FLIGHT SYSTEM DESIGN

While it was not a focus of this study to develop a complete spacecraft design for a specific science mission concept, in order to address the key mission risks identified in Section 1 it was important to constrain the potential mass and volume of the flight system to be delivered by the aerocapture system. This was also necessary to confirm that the components required to successfully execute a deep space SmallSat science mission could be accommodated within the constraints of the aerocapture system.

The layout of the internal components in the notional system can be seen in Figure 19. This shows the spacecraft that
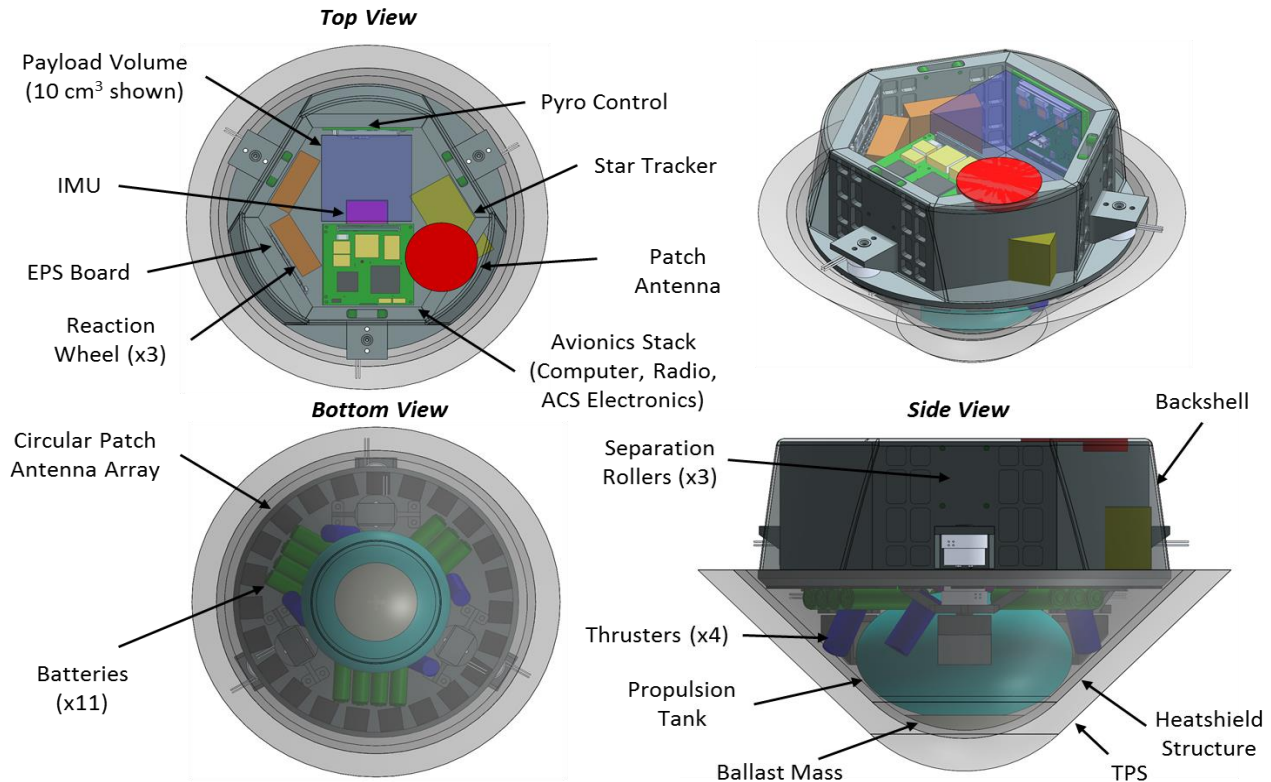

Figure 19. Notional flight system internal component layout

12

would exit the atmosphere and enter orbit. The drag skirt is not present, as it would have been jettisoned during the pass through the atmosphere to provide control in targeting the desired science orbit. A mass summary for the entire notional aerocapture flight system can be seen in Table 6. This mass summary reflects a fully margined system with contingencies applied to each subsystem, accounting for the early stage that this design is currently in and leaving room for generous growth as the mission concept is refined further. All of the prior simulation results shown were generated with this fully margined mass, providing conservative estimates.

The flight system would have all of the components necessary to complete a deep space SmallSat science mission successfully. The nose would contain a micro-propulsion system to perform the critical periapsis raise maneuver after aerocapture. The heatshield would be jettisoned after the maneuver to expose the thrusters. This system could also provide 3-axis control to desaturate reaction wheels. Also in the nose are Lithium-ion battery cells to provide power to the spacecraft during the approximately 24 hour coast phase after jettison from the host spacecraft, but before entering the atmosphere. These batteries would continue to provide energy to the flight system during high power modes, such as telecommunication downlink, during the orbital phase of the mission. They would be charged by solar cells.

Table 6. Notional flight system mass summary

Mass Summary	CBE kg	Contingency %	MEV kg
Flight System	24.9	23%	30.7
Payload	4.7	30%	6.1
Spacecraft Bus	20.2	22%	24.6
Power	1.8	18%	2.1
C&DH	0.2	30%	0.3
Telecom	1.9	15%	2.1
Structure	6.7	28%	8.6
Deployment Mechanisms	3.4	20%	4.0
Thermal	1.8	25%	2.3
Propulsion	1.4	20%	1.6
GN&C	2.4	17%	2.8
Cabling	0.7	15%	0.8
Drag Skirt	22.0	41%	30.9
Flight System (margined)			35.5
Drag Skirt (margined)			31.5
Margin			43%
Dry Mass Allocation			67.0
Total Propellant			1.3
Propellant			1.3
Total Launch Mass			68.2

The aluminum hexagon structure that contains the avionics and science payload would provide shielding from the radiation environment. Space is allocated for a rad-hard computer and X-band Iris radio, similar to what has been flown on MarCO [20]. A circular patch array antenna would provide a space-efficient way to accommodate a system capable of communicating through the Deep Space Network. The attitude control system includes three reaction wheels for fine pointing control, a star tracker, and an IMU. Space is also allocated for the necessary control electronics to control and activate the various separation mechanisms for the drag skirt,

heatshield, and backshell, which are discussed in more detail in Section 8.

While a specific science payload is not included at this time, Figure 19 shows that there is space for an instrument of approximately 10x10x10cm, or "1U", with additional space for payload electronics throughout the system. With more detailed science and instrument requirements the entire flight system can be optimized, but this demonstrates that the system can accommodate a number of CubeSat/SmallSat scale instruments that are currently being developed and considered for mission concepts, such as imagers, spectrometers, and field sensors.

8. MECHANICAL SYSTEM DESIGN

Structural Design and Analysis

An aerocapture small satellite requires some unique mechanical design choices when compared to typical SmallSats because it must survive passage through the atmosphere at hypersonic velocities. Principally, the flight system must be packaged into an aeroshell with ablative TPS. The side view in Figure 19 shows how the heatshield of the vehicle could be configured. It is made up of a carbon fiber laminate structure with C-PICA TPS, determined by the analysis described in Section 6. The drag skirt is composed of two aluminum facesheets with a honeycomb core to decrease mass while retaining stiffness. This structure is also covered with C-PICA TPS.

Preliminary finite element analysis was conducted to assess the structural integrity of these systems. Under 20g max deceleration, well above the 11g maximum expected from the analysis described in Section 5, both the heatshield and drag skirt are expected to remain structurally intact with 0.1 mm maximum deflection. The first mode of the heatshield is expected to be approximately 450 Hz and the first mode of the drag skirt is expected to be approximately 69 Hz.

Separation System Design

Also important for the success of the aerocapture system is that the drag skirt separates accurately and cleanly during atmospheric flight at the required time to target the desired science orbit. To ensure that the drag skirt does not recontact the spacecraft during the separation event, which could make the spacecraft unstable, a rail and roller system was designed. The details of this system can be seen in Figure 20, where the drag skirt is depicted as it would be at the end of the jettison event.

The three rails would fit into rollers embedded in the walls of the hexagon structure, shown in Figure 19. Three NEA Model 9100 Hold Down and Release Mechanisms [21] hold the drag skirt onto the spacecraft. These release mechanisms are non-pyro and low shock, which minimizes the risk of damage to the spacecraft components mounted close by. In the most conservative case, each mechanism is expected to need to hold approximately 3.92 kilonewtons of force, well below

their 6 kilonewton load rating. The same mechanisms could be used to detach the heatshield and backshell, but these separation events occur after the vehicle has exited the atmosphere and entered orbit. The separation of these pieces exposes the spacecraft components.
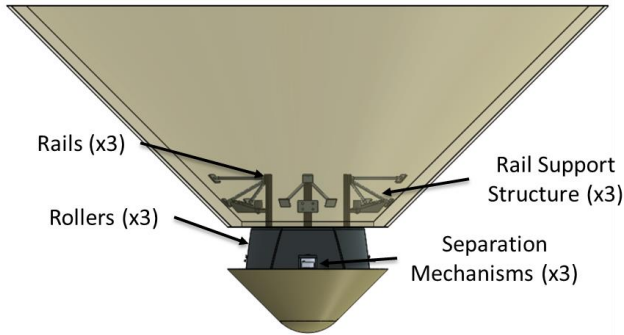

Figure 20. The mechanical separation system includes guide rails to ensure a clean jettison of the drag skirt

9. AERODYNAMICS ANALYSIS FOR MULTI-BODY SEPARATION

Motivation and Background of CFD Simulations

Although single-event-jettison drag modulation is a promising and straightforward control option, there may be risks associated with the maneuver. Prior investigations into drag-modulated aerocapture have not studied the separation event in depth, and the existing literature on hypersonic jettison events is sparse. Modeling the dynamics of the drag modulation event will help characterize its risks, including potential near and far-field recontact between the drag skirt and the spacecraft body, and instability of the spacecraft body following separation.

A series of computational fluid dynamic (CFD) simulations were used to model aerodynamic and dynamic interactions associated with the separation event. The Cart3D simulation package was selected for these simulations [22]. Cart3D includes a second-order Euler solver that discretizes the governing equations over multi-level Cartesian meshes. Cart3D has been used previously for both hypersonic [23] and multi-body studies [24]. The simulation package has a number of features that make it beneficial for preliminary aerodynamic design, including automatic adaptive mesh refinement and the option to produce time-dependent, component-wise aerodynamic simulations for multi-body vehicles.

As Cart3D uses an inviscid flow solver, the effects of viscosity in these simulations are neglected. With that said, these models still convey valuable information about the inertial aerodynamic forces experienced by the vehicle, in a flight regime where these forces are likely dominant for blunt bodies due to the high Reynolds numbers experienced [25]. The accuracy of these simulations is therefore suitable for this preliminary design phase, given their minimal computational cost.

Static Aerodynamics

A series of steady-state Cart3D simulations were performed at the nominal jettison point of the spacecraft's baseline trajectory. These simulations were used to generate aerodynamic coefficients for the vehicle both before and after the jettison of the drag skirt. Table 7 shows the atmospheric values and trajectory conditions at which these simulations were run. The angle of attack, α, was varied by increments of 5 degrees. The reference density, ρ_∞, was obtained from a simulation of the baseline trajectory. The specific heat ratio, γ, was obtained from Reference 26.

Figure 21 shows the resulting lift and drag coefficients for each case after drag skirt jettison. These results are plotted against values from CBAERO, a Modified-Newtonian inviscid flow solver [27], for validation. Both software packages produce similar coefficients, although Cart3D predicts lower values for C_D and less variability in C_L than CBAERO.

Table 7. Conditions for Steady-State Aerodynamic Simulations

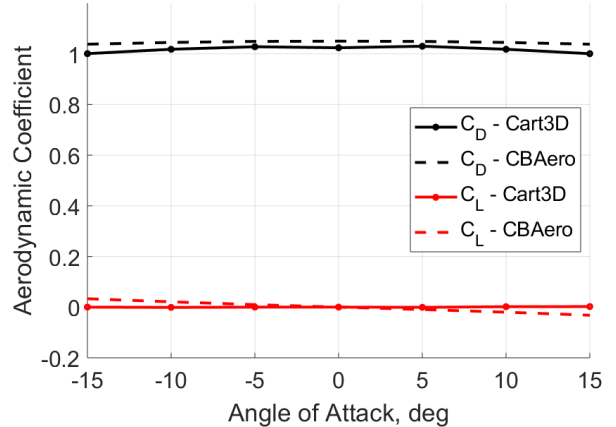| Parameter	Value
Mach	40
α	-15 deg < α < 15 deg
ρ_∞	$1.064 \cdot 10^{-4}\,\text{kg/m}^3$
γ	1.286

Figure 21: Comparison of Aerodynamic Coefficients between Cart3D and CBAERO

The flow solution produced by Cart3D for the 0-degree α case is shown in Figure 22, with contours representing the square root of the ratio of atmospheric density to reference density, $\sqrt{\rho/\rho_\infty}$. In this simulation, seven adaptive mesh refinements were performed. The iterative convergence behavior for the configuration with the drag skirt attached is shown in Figure 23, where the objective function J_H represents the sum of C_D and C_L. The changes in this function become very small as Cart3D runs more multigrid cycles, indicating convergence of the aerodynamic coefficients on the later meshes. The final mesh for this configuration contains 8,969,766 cells.
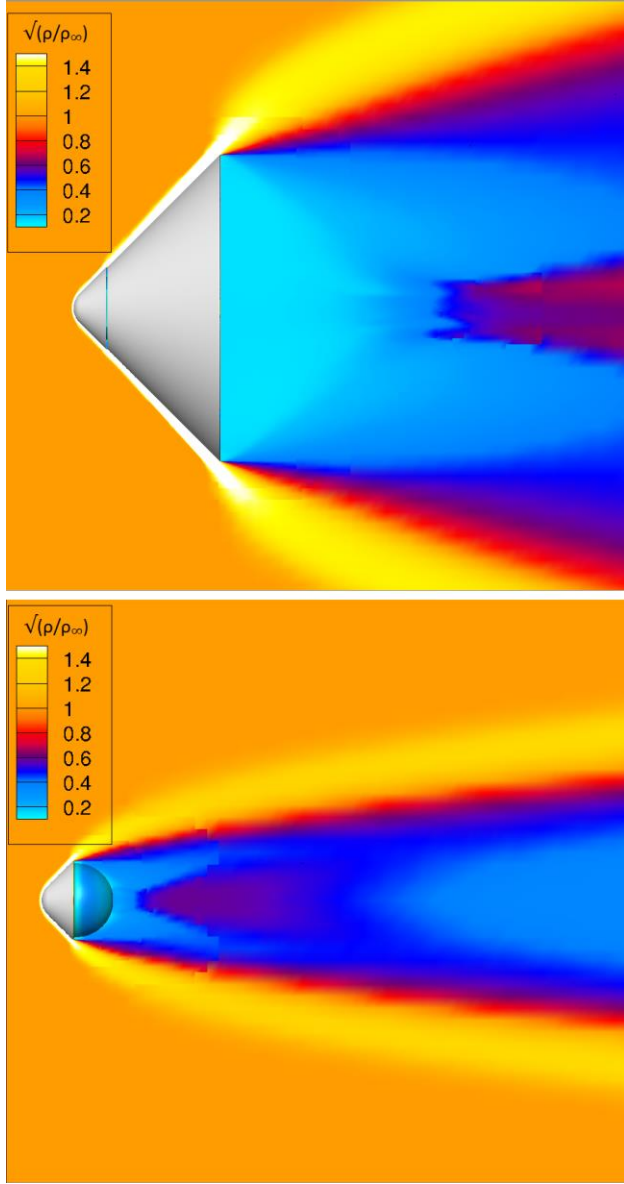
14

Figure 22: Flow Solutions for Configuration With (top) and Without (bottom) Drag Skirt Attached
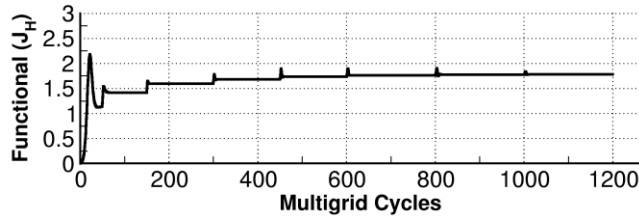

Figure 23: Cart3D Iterative Convergence Behavior for Configuration With Drag Skirt Attached

The Cart3D aerodynamic coefficients for this 0-degree α case are provided in Table 8, where Configuration 1 represents the vehicle with the drag skirt attached, and Configuration 2 represents the spacecraft body after the drag skirt is jettisoned.

Table 8. Aerodynamic Coefficients for Nominal Trajectory

Configuration 1		Configuration 2	
C_D	C_L	C_D	C_L
1.0127	0.0021	1.0284	0.0009

Dynamic Simulations

To analyze the risks of recontact and spacecraft instability following the drag skirt jettison event, a series of dynamic simulations were performed. The dynamics of the separation event were modeled using a built-in 6-DOF motion integrator in Cart3D. This 6-DOF model assumes that the only loads acting on the body are aerodynamic, and that the momentum transferred from the fluid to the body is much greater than that transmitted to the fluid by the moving body. The latter assumption becomes more accurate for objects with large ballistic coefficients, such as the spacecraft body after drag skirt separation. The 6-DOF integrator solves the Newton-Euler equations for rigid-body motion, with propagation performed between subsequent flow solutions. This approach utilizes quasi-steady aerodynamics, where flow values do not change during each motion propagation period. As a result, the 6-DOF model cannot predict dynamic stability behavior. Further information about this integrator, as well as validation results, can be found in Appendix A of Reference 24.

The dynamic simulations developed in this study use simplified versions of the baseline spacecraft geometry. Smaller features, such as the separation system, have been removed, and the flight system is modeled as a solid body with a uniform mass distribution. Major parameters, such as the dimensions of the outer faces of the vehicle and the location of the center of mass, are consistent with the notional design.

A full-factorial test matrix was run to probabilistically constrain the risk of an off-nominal drag skirt jettison for a range of potential flight conditions. The simulation inputs for these tests are shown in Table 9. For this test matrix, Mach and α were varied, with increments of ΔM = 10 degrees and Δα = 2 degrees.

Table 9. Test Matrix for Potential Flight Conditions

Parameter	Value
Mach	30 < Mach < 50
α	0 deg < α < 5 deg
Δt	0.015 s
t_{tot}	1.5 s
ρ_∞	$1.064 \cdot 10^{-4}\,\mathrm{kg/m^3}$
γ	1.286

Figure 24 shows the separation sequence for the baseline trajectory, where M = 40 and α = 0 degrees. Similar to the

static simulations, the contours in these images represent the square root of the ratio of atmospheric density to reference density, $\sqrt{\rho/\rho_\infty}$. From these images and from the 6-DOF motion data provided by the simulations, the drag skirt and the flight system do not appear to be at risk of recontact in the near-field (due to the separation motion being almost purely horizontal) or in the far-field (due to the large deceleration difference between the two bodies, which causes them to separate quickly). Results from the test matrix further indicate that this separation event occurs without risk of recontact for a range of potential flight conditions. One potential cause for concern is the growth of pitch angle in the post-jettison vehicle for some of the flight condition combinations. However, the simulations did not include dynamic stabilizing effects (such as pitch damping) or a spin-rate on the vehicle, which could help to increase stability. Further work is needed to identify the cause and impact of these dynamics.

An additional set of dynamic simulations was run to provide validation data that can be compared against the ballistic range testing discussed in Section 11. Conditions for these cases are provided in Table 10. The chosen β-ratios and Mach number correspond to the planned conditions for the ballistic range tests. The β-ratio was altered by adjusting the mass of each spacecraft component within the dynamic simulation while holding the dimensions of the components constant. When compared to results from the prior test matrix, the drag skirt takes longer to fully separate from the flight system body within these simulations, due to the smaller difference in ballistic coefficients after separation and the lower Mach number. With that said, each jettison still occurs cleanly for each configuration. By comparing these simulations to results from the ballistic range tests, the accuracy of this dynamic model and the probabilistic risk results can be assessed.

Table 10. Test Matrix for Ballistic Range Validation

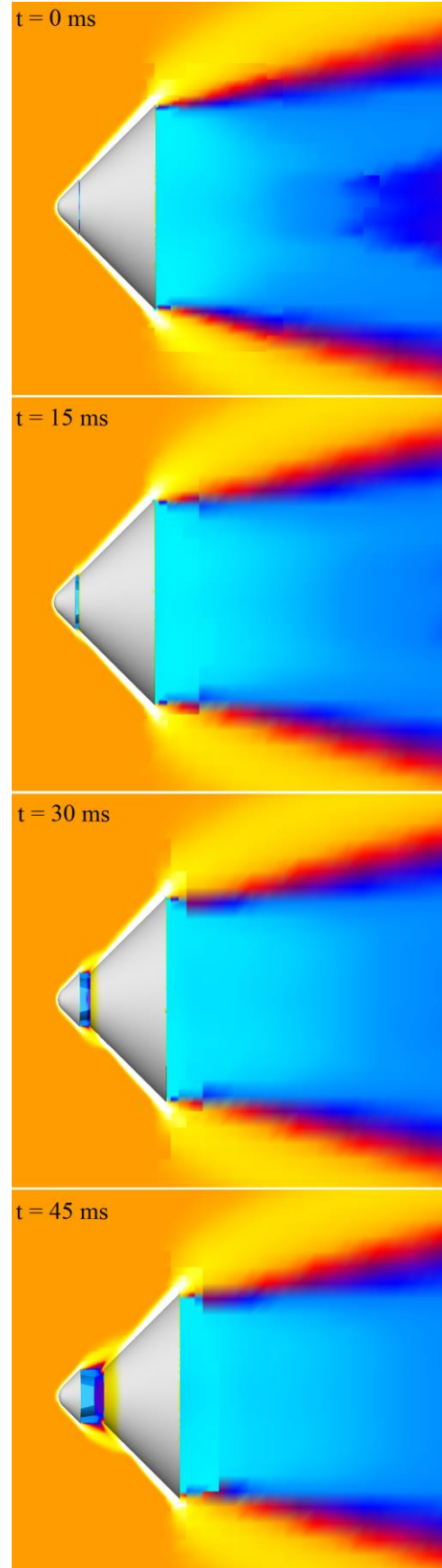| Parameter	Value
Mach	10
α	0 deg
Δt	0.010 s
t_{tot}	1.5 s
ρ_∞	$1.064 \cdot 10^{-4}\,\mathrm{kg/m^3}$
γ	1.29
β-ratio	1.36, 3.38, 4.68

Figure 24. Skirt Separation Sequence for M = 40, α = 0°

10. CONCLUSIONS

The results of this study indicate that a SmallSat aerocapture system could be feasible and can provide substantial mission benefits, when compared to propulsive orbit insertion. Figure 25 shows a comparison of the mass efficiency for the aerocapture system versus propulsive orbit insertion for a number of different orbit apoapsis altitude targets. Mass efficiency is expressed as the amount of delivered mass to orbit for a 68 kg total mass spacecraft. The delivered mass to orbit is the maximum mass of the spacecraft used for the science mission. It can be seen that the aerocapture system delivers 26 kg to all orbits, while the propulsive options deliver less mass for all orbits with an apoapsis less than about 20,000 km altitude. This is because the amount of propellant needed for the orbit insertion maneuver increases as the orbit apoapsis decreases, but the aerocapture system is the same mass regardless of target orbit. Regardless of orbit apoapsis altitude, designing and integrating a propulsion system to perform hundreds to thousands of meters per second delta-V on a small platform is potentially difficult and risky, making aerocapture a viable method for OI at all orbits.
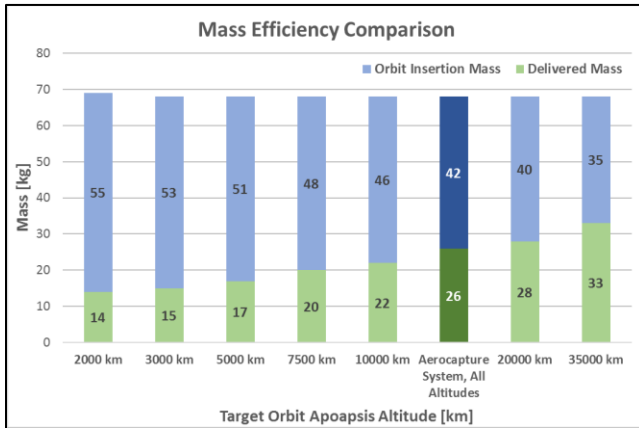

Figure 25. When compared to propulsive OI, the aerocapture system can deliver 50-85% more useful mass for orbits ranging from 5000 km down to 2000 km

This study has successfully addressed all three of the key challenges identified in Section 1 for a SmallSat aerocapture spacecraft. Vehicle stability throughout atmospheric flight has been modeled with preliminary CFD simulations. These show that there may be a stability issue after jettison with the spacecraft, but ongoing work to refine the simulations will address this issue and consider how adding a spin-rate to the flight system might provide more resiliency. Simulations show that the risk of recontact during the drag skirt jettison event is likely minimal, but a rail and roller separation system has also been integrated into the design to ensure that this is not an issue in flight.

A robust simulation toolkit has been developed to model the vehicle during flight through the atmosphere and assess the effects of navigational and atmospheric uncertainties. A set of Monte Carlo simulations demonstrate that the spacecraft could target a desired orbit with enough accuracy for a science mission. In addition, aerothermal stresses have been analyzed to determine that well characterized TPS materials, such as PICA and C-PICA, are adequate for this mission.

This study has concluded that aerocapture for SmallSats could be a viable way to increase the delivered mass to Venus and could also be used at other destinations. With increasing interest in SmallSats and the challenges associated with performing OI burns on small platforms, this technology could enable a new paradigm of planetary science missions.

11. FUTURE WORK PLANNED

The study team has plans to continue development of aerocapture technology for SmallSats, including additional CFD simulations to assess stability in the atmosphere and modeling to address how adding a spin-rate to the flight system can aid in stability. Ballistic range tests are also planned for mid-2019 at NASA's Ames Research Center. These tests will address the stability of the spacecraft and also image the drag skirt jettison event to validate that a clean separation would occur. Several exploratory tests were performed in 2018 to demonstrate this approach. Images from these tests that show the spacecraft separating from the drag skirt can be seen in Figure 26. The mid-2019 tests will be performed in a similar manner, but with a spacecraft design based on the notional system presented here in order to provide a comparison to the completed simulations.

The study team is also pursuing a design iteration to utilize the ADEPT deployable drag skirt. This system could allow the spacecraft to stow into a much smaller volume to provide more flexibility for secondary launch opportunities.

Finally, candidate science missions are being assessed that fit well with the aerocapture technology concept to pursue a more complete spacecraft design to meet science requirements. In the future, it is envisioned that aerocapture could be the orbit insertion method of choice for small spacecraft, such as those proposed under NASA's SIMPLEx program, as well as feeding forward to larger aerocapture missions.
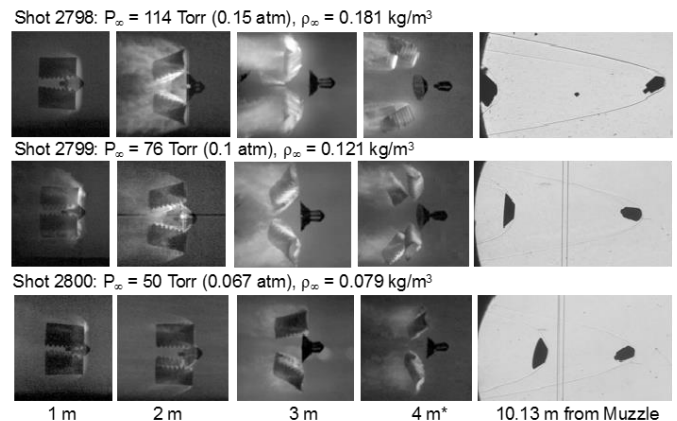

Figure 26. Ballistic range test shots were completed, demonstrating the applicability for aerocapture

REFERENCES

[1] Walberg, G. D., "A Survey of Aeroassisted Orbit Transfer", Journal of Spacecraft and Rockets, Vol. 22(1), 1985

[2] Hall J. et al., "Cost-Benefit Analysis of the Aerocapture Mission Set", Journal of Spacecraft and Rockets, Vol. 42(2), 2005

[3] Rohrschneider, R. R. and Braun. R., "Survey of Ballute Technology for Aerocapture", Journal of Spacecraft and Rockets, Vol. 44(1), 2007

[4] Lockwood M. K., AIAA/ASME/SAE/ASEE Joint Propulsion Conference and Exhibit, 2003

[5] Zachary R. Putnam, and Robert D. Braun, "Drag Modulation Flight Control System Options for Planetary Aerocapture", Georgia Institute of Technology, Atlanta, Georgia, 30332

[6] Werner, M. S. et al, "Development of an Earth SmallSat Flight Test to Demonstrate Viability of Mars Aerocapture", 55th AIAA Aerospace Sciences Meeting, AIAA 2017-0164, 2017

[7] K. C. Clausen et al, "The Huygens Probe System Design", Space Science Reviews, Kluwer Academic Publishers, 2003

[8] Venkatapathy, E.; et al, "Adaptive Deployable Entry and Placement Technology (ADEPT): A Feasibility Study for Human Missions to Mars" 21st AIAA Aerodynamic Decelerator Systems Technology Conference, AIAA 2011-2608

[9] Smith et al., "Nano-ADEPT: An Entry System for Secondary Payloads," IEEE Aerospace Conference, Big Sky, MT, March 2015.

[10] "JPL MarCO – Micro CubeSat Propulsion System", Product Brief, VACCO, South El Monte, California, 2014

[11] "Lunar Flashlight Propulsion System", Product Brief, VACCO, South El Monte, California, 2017

[12] Carolyn Mercer, "Planetary Science Deep Space SmallSat Studies", Lunar Planetary Science Conference Special Session, The Woodlands, Texas, March 18, 2018

[13] J. Balaram, et al., "DSENDS -A High-Fidelity Dynamics and Spacecraft Simulator for Entry, Descent and Surface Landing", IEEE 2002 Aerospace Conf., Big Sky, Montana, March 9-16, 2002.

[14] "Pioneer Venus Program", Hughes Aircraft Company Space and Communications Group, June, 9 1976.

[15] Venus-Global Reference Atmospheric Model (Venus-GRAM 2005)", NASA Marshall Space Flight Center Environments Group, EV44, AL 35812

[16] "Ultra High Performance Inertial Measurement Unit (IMU)", STIM300 Product Brief, Sensonor AS, Horten, Norway.

[17] Hillary L. Justh, "Global Reference Atmosphere Model (GRAM) Overview", GRAM Virtual Workshop, Sep. 21, 2017, Natural Environments Branch NASA Marshall Space Flight Center, AL 35812

[18] Allen Jr, G.A., Wright, M.J, and Gage, P., The Trajectory Program (TRAJ): Reference Manual and User's Guide, NASA/TM-2005-212847, March 2005.

[19] Milos, F. S., and Chen, Y.-K., "Ablation, Thermal Response, and Chemistry Program for Analysis of Thermal Protection Systems," Journal of Spacecraft and Rockets, Vol. 50, No. 1, 2013, pp. 137–149

[20] M. Michael Kobayashi, "Iris Deep-Space Transponder for SLS EM-1 CubeSat Missions", 31st Annual AIAA/USU Conference on Small Satellites

[21] "NEA Model 9100 Hold Down & Release Mechanism", Product Brief, NEA Electronics, Moorpark, California, 2014

[22] Aftosmis, M. J., et al., "A Parallel Multilevel Method for Adaptively Refined Cartesian Grids with Embedded Boundaries," 38th Aerospace Sciences Meeting and Exhibit, Reno, NV, AIAA 2000-808, January 2000.

[23] Tancred, J. A., and Rumpfkeil, M., "Aerodynamic Response Quantification of Complex Hypersonic Configurations using Variable-Fidelity Surrogate Modeling," 53rd AIAA Aerospace Sciences Meeting, Kissimmee, FL, AIAA 2015-1703, January 2015.

[24] Murman, S. M., Aftosmis, M. J., and Berger, M. J., "Simulations of 6-DOF Motion with a Cartesian Method," 41st AIAA Aerospace Sciences Meeting, Reno, NV, AIAA 2003-1246, January 2003.

[25] Schneider, S. P., "Laminar-Turbulent Transition on Reentry Capsules and Planetary Probes," Journal of Spacecraft and Rockets, Vol 43, No. 6, 2006, pp. 1153-1173.

[26] Hammer, M., "Atmosphere of Venus", University of Arizona, Tucson, AZ, 2017 (unpublished).

[27] Kinney, D., "Aero-thermodynamics for conceptual design," 42nd AIAA Aerospace Sciences Meeting and Exhibit, American Institute of Aeronautics and Astronautics, Reno, NV, January 2004.

BIOGRAPHY

Alex Austin is a Systems Engineer in the Advanced Design Engineering group at JPL, where he works on new mission concept formulation and proposals in all areas of space exploration. His recent work has focused on innovative concepts for performing planetary science with SmallSats. He received a bachelor's degree in Aeronautical and Mechanical Engineering and a master's in Aeronautical Engineering from Rensselaer Polytechnic Institute.

Adam Nelessen is a Systems Engineer at JPL, where he focuses on the design and architecture of EDL systems. Adam is an EDL Systems Engineer for the Mars 2020 mission, as well as the Principal Investigator for a Technology Development initiative examining the use of aerocapture to deliver Small Satellites to orbit. He received a JPL Voyager Award for his work in the formulation of future Mars Sample Return missions. He holds a B.S. degree in Mechanical Engineering from Northern Arizona University, and a M.S. degree in Aerospace Engineering from the Georgia Institute of Technology.

Dr. Ethiraj Venkatapathy is currently the Senior Technologist for Entry System Technologies at NASA Ames Research Center and the Project Manager for the Advanced TPS Materials (TPSM) development for the Game Changing Development Program of the Space Technology Mission Directorate, NASA HQ. He is an Associate Fellow of Ames and an Associate Fellow of AIAA. He obtained his Ph.D. from Iowa State University in Aerospace Engineering and his Bachelor of Technology from Indian Institute of Technology, Madras, India.

Dr. Robert D. Braun is the Smead Professor of Space Technology and the Dean of the College of Engineering and Applied Science at the University of Colorado Boulder. He leads an active research program focused on the design of advanced flight systems and technologies for planetary exploration and has contributed to the formulation, development, and operation of multiple space flight missions. From 2003 to 2016, he served as a faculty member at the Georgia Institute of Technology. Prior to joining the Georgia Tech faculty, Dr. Braun was a member of the technical staff of the NASA Langley Research Center for 16 years. He served as the NASA Chief Technologist in 2010 and 2011.

Bill Strauss is an engineer at the Jet Propulsion Lab working in the Entry Descent and Landing GN&C Systems Group. He has worked at JPL for 17 years and has a total of 23 years experience in the Aerospace Industry. He received his M.S. in Engineering Mechanics and Astronautics from the University of Wisconsin Madison in 1994.

Josh Ravich is a Mechanical Engineer in the Technology Infusion group at JPL, where he works on the mechanical design and analysis of spacecraft systems. His recent work has included the Mars Helicopter project. He received a bachelor's degree in Mechanical Engineering from UC Berkeley and a master's in Mechanical and Aerospace Engineering from the University of Michigan.

Mark Jesick is a Mission Design Engineer in the Inner Planet Mission Analysis group at JPL. He earned his B.S. in Aerospace Engineering from the University of Notre Dame, and his M.S. and Ph.D. in Aerospace Engineering from The University of Texas at Austin.

Robin A. S. Beck has been a member of the limited group of U.S. experts on developing, designing, testing, and modeling ablative materials for use in earth and planetary entry, rocket nozzle exhausts, and laser environments for over 35 years. After spending over 20 years in industry, Ms. Beck joined NASA Ames Research Center in 2006. She was appointed to the Mars Science Laboratory (MSL) team as Cognizant Engineer (Cog-E) for the MSL Thermal Protection System (TPS). After MSL successfully landed the Curiosity Rover on Mars, Ms. Beck became the technical lead of the CA-TPS element of the TPSM project. Ms. Beck is currently the Mars 2020 TPS Cog-E, reprising her role from MSL. She received a BSME from Santa Clara University, an MSME from Stanford University and she is an Associate Fellow of the AIAA.

Paul Wercinski received a B.S. in Aerospace Engineering from the Pennsylvania State University in 1987 and a M.S in Aero/Astro Engineering from Stanford University in 1990. He has been with the NASA Ames Research Center for more than 30 years. He is currently the project manager for the Adaptable, Deployable Entry and Placement Technology (ADEPT) project since 2012. He has been involved in multiple areas within the Entry, Descent, and Landing (EDL) discipline at NASA over the past several decades. He had served a 1-year assignment at NASA HQ in the Science Mission Directorate as program executive for the In-Space Propulsion Technology Program (2002-2003). He has served in line management roles at NASA Ames as well as participating in numerous planetary mission studies with an emphasis on EDL.

Michael J. Aftosmis is an Aerospace Engineer in the NASA Advanced Supercomputing Division at Ames Research Center in northern California. His work focuses on the development and application of numerical methods for computational fluid dynamics and the application of advanced simulation techniques to the design and analysis of space launch vehicles and advanced aircraft. Michael leads NASA's Cart3D software development team which supports a community of over 600 users across all NASA mission directorates, the DoD, DOE, academia and industry. In 2014 he received NASA's Exceptional Engineering Achievement Medal. His work has been recognized through numerous awards from NASA, the US Air Force, the AIAA and the Russian Federal Space Agency. He holds a S.M. in Aerospace Engineering from MIT, a B.S. from Syracuse University and is an Associate Fellow of the AIAA.


Michael Wilder is a senior research engineer in the Aerothermodynamics branch at NASA Ames Research Center, where he utilizes the hypersonic ballistic range to conduct experimental investigations into the aerodynamics and aerothermo-dynamics of atmospheric entry. Recent work has focused on the effects of surface roughness on boundary-layer transition and heat transfer during atmospheric entry at Mars, Venus, and the outer planets. He received his Ph.D. in engineering science from Virginia Tech and his B.A. in physics/astronomy from the University of Virginia. He is an Associate Fellow of Associate Fellow of AIAA.

Gary A. Allen, Jr. is an aerospace engineer employed by Analytical Mechanics Associates, Inc., an onsite contractor at NASA Ames Research Center. He received a Bachelor of Science in Engineering Physics degree from the University of California, Berkeley, and Ph.D. in Aerospace Engineering from Stanford University, California. His main professional focus is modeling and simulation of spacecraft atmospheric entry through engineering approximations. Dr. Allen is the author of the Traj atmospheric entry and thermal protection simulation program. Through use of Traj, Dr. Allen has participated at NASA Ames in many pre-Phase—A-Studies for missions to most of the Solar System's planets and played a significant role in sizing the thermal protection system for the Mars Exploration Rover (MER) aeroshell.
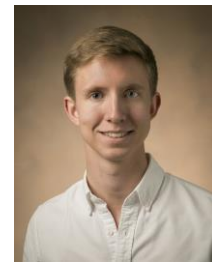
Michael Werner is a graduate research assistant in the Colorado Center for Astrodynamics Research at CU Boulder, and a NASA Space Technology Research Fellow. His research work focuses on demonstrating the viability of aerocapture with SmallSats. He received his B.S. in Mechanical Engineering from the Colorado School of Mines, and his M.S. in Aerospace Engineering from the Georgia Institute of Technology.

Evan Roelke is currently a Graduate Research Assistant at CU Boulder in the Colorado Center for Astrodynamics Research (CCAR). He obtained a B.S. in Mechanical Engineering from Brown University and an M.S. in Aerospace Engineering from the Georgia Institute of Technology. His current research interests include GNC algorithm assessment for discrete-event, drag-modulated aerocapture systems.